PARAMETRIC ANALYSIS OF PRESTRESSED CONCRETE BEAMS WITH THE FINITE ELEMENT METHOD

Brwa BEBANI[1], Mieczysław KUCZMA[1*], Krzysztof ZIOPAJA[2]
[1]Institute of Building Engineering, Poznan University of Technology, Poznań, Poland
[2]Institute of Civil Engineering, Poznan University of Technology, Poznań, Poland

A b s t r a c t

This study presents a numerical analysis of a prefabricated prestressed concrete beam subjected to a three-point bending test. The beam has a span length of 4600 mm and cross-section of 240 x 400 mm, and was prestressed with a single 7-wire strand with a diameter of 15.2 mm. In order to ensure the propriety and reliability of the numerical model of the studied beam, a parametric analysis of the influence of selected model components on the determined results was carried out. Using the finite element method (FEM) software Abaqus/CAE by Simulia, the following parameters were analyzed: a) the effect of mesh size and meshing method, b) the type and shape of elements, c) the method of transferring the prestressing force, d) the effect of passive reinforcement. To check the reliability and effectiveness of the model, the obtained numerical results were compared and contrasted with analytical solutions, assessing the sensitivity of FEM factors. The results presented in the paper demonstrate high agreement between numerical simulations and analytical calculations for the prestressed concrete beam, encompassing the deflection and stresses in both the elastic and characteristic states of inelastic ranges.

Keywords: parametric and numerical analysis, analytical solution, meshing strategy, Abaqus/CAE, Magnel diagram

1. INTRODUCTION

Concrete is the most popular construction material because of its many advantages, including local availability of components, undemanding manufacturing process, the possibility of producing structural elements of any shape, as well as good mechanical and physical properties, in particular, compressive strength and high durability and many pro-sustainable features, see Brandt [1], Mehta and Monteiro [2], Mosley *et al*. [3]. The main shortcomings of concrete are its low tensile strength, about ten times smaller than its compressive strength, and its semi-brittle nature that makes concrete prone to the development of cracks, which reduce the stiffness, load-bearing capacity, and service life of concrete structures. In order to mitigate the effect of lower tensile strength, prevent cracking, and increase the load-bearing

---

[1]*Corresponding author: Institute of Building Engineering, Poznan University of Technology, Pl. M. Skłodowskiej-Curie 5, 60-965 Poznan, Poland, mieczyslaw.kuczma@put.poznan.pl, +48616652155

capacity of concrete structures, the concept of prestressing concrete is applied. The calculation and design of prestressed concrete structures are challenging due to the concrete's complex microstructure, creep phenomena, shrinkage, chemical hydration, and evolution of self-equilibrated micro-stresses occurring in concrete over time, Ulm *et al.* [4]. In particular, the rheological effects are decisive and must be carefully considered in the design of prestressed concrete structures, Ajdukiewicz and Mames [5], Knauff and Niedośpiał [6].

Nowadays, the determination of internal forces in concrete structural elements is facilitated by computer programs. However, solving a boundary value problem in the inelastic range due to the softening behaviour of concrete, which is a result of cracking, remains still a challenge because the problem becomes ill-posed in the mathematical terms. Using the finite element method to analyze concrete structures, both reinforced and prestressed, has become an essential tool for today's researchers and advanced designers. This is especially true in the analysis of unconventional problems and optimization. The significant development of the FEM and its applications to solving various engineering problems has been observed since the 1960s, Zienkiewicz *et al.* [7].

A new approach to concrete analysis is provided by Hillerborg *et al.* [8], who combines fracture mechanics and FEM taking into account crack formation, and propagation, as well as failure. In particular, solving incrementally the nonlinear model, which takes into account crack formation and propagation along with the material's tensile strength and physical characteristics, has enabled a more realistic and reliable representation of stress states and crack distribution, including the mechanisms of failure. Nowadays, numerical simulations have the unquestionable feature that they allow simultaneous analysis of the effects of many different factors on the designed component and thus reduce expensive and time-consuming laboratory experiments. Among commercial FEM programs, Abaqus/CAE is known for its practicality and potential, and its application can be found in references [9, 10, 11]. Al-Hilali and Izzet [9] present the findings of numerical analyses and experimental tests conducted on six prestressed I-beams with various holes in the web. Yapar et al. [10] modeled a scheme developed to capture the actual mechanics of a precast prestressed concrete beam across all stages of loading—manufacture, service, and limit state—and validated through laboratory tests. Lee *et al.* [11] discuss the results of numerical analyses performed for twenty prestressed beams with an external tendon profile while considering various parameters in FEM simulations. Wang *et al.* [12] studied the fire resistance of prestressed concrete T-beams using numerical simulations, taking into account the effects of various fire modes, concrete strengths, cover and protective layer thicknesses, and prestressing levels.

A widespread group of designers and scientists emphasize that in EN 1992-1-1 [13], there is no clear classification of prestressed structures according to the degree (intensity) of prestressing. Only general rules for the design of prestressed elements are given, and limit conditions for characteristic normal stresses in concrete and prestressing steel are defined. Monographs [3, 5, 6] have discussed the characteristic behavior of prestressed structures, delving into the physical phenomena associated with prestressing and their mathematical representations. These studies segmented the analysis of prestressed structures into three stages: i) the initial stage, where the element is completed and prestressed; ii) the unserviceable state, encompassing immediate and delayed losses of prestressing force and the constant load reached its full value; iii) the service stage, where the service load is fully applied, while the value of the prestressing force is reduced by ad hoc and delayed losses. It is important to mention that the basis of the harmonized national standards was a joint initiative of the CEB and FIP organizations, started in the 1960s, providing the fundamental trends and directions for studying concrete structures [14].

Obtaining reliable results from numerical analyses is a primary goal when developing structural models. This minimizes the need to make and test many different sample specimens for examination, which is a standard activity in the initial design stage. Improved numerical models can be adapted in subsequent studies as long as they are universal and thus valuable for the field. Numerical simulations

of prestressed concrete elements require consideration of various mechanical and technical aspects so that their models can realistically reflect the behavior of these structures at various stages of manufacturing, prestressing, and in-service. The process can be difficult and time-consuming, as it relies on a number of parameters, such as the material model, boundary conditions, mesh size, mesh generation techniques, prestressing techniques, the effects of bonding and adhesion force distribution at the interface of concrete and prestressing strands, or the load-bearing capacity of the connections between precast elements and in-situ concrete.

Detailed computational methods utilize finite element principles to model the distribution of forces at the tendon-concrete interface and design the anchorage zone in pre-tensioned concrete elements referenced in [15, 16]. The relationships between bond stress-slippage depend on various important factors, such as the strength and composition of the concrete mix, method of concreting and maturity conditions, thickness of concrete cover, type of prestressing tendons, stress state in tendons, and technology of prestress release. These issues are critical and complex in numerical modeling; hence, they are still being addressed and are expected to be in future publications. Understanding the constitutive laws governing elastic response, elastic-plastic phenomena, fracture mechanics, and failure is essential for analyzing concrete structures. This knowledge is crucial for grasping concrete's nonlinear behavior, where the determination of stress-strain curves encounters many difficulties.

For this reason, Lubliner *et al*. [17] developed a novel plastic-damage model for concrete, further advanced by Lee and Fenves [18] — the concrete damaged plasticity (CDP) model, by using the concepts of fracture-energy-based damage and stiffness degradation in continuum damage mechanics. Two damage variables, one for tensile damage and the other for compressive damage, and a yield function with multiple hardening variables are introduced to account for different damage states. The CDP model exhibits many advantageous features in numerical analyses of the non-homogeneous and non-linear mechanical behaviour of concrete, accounting for strain softening, which is defined as decreasing stress with increasing deformations, in both compression and tension. The state-of-the-art of CDP models and the procedure for identifying the constitutive parameters are presented in [19, 20]. A similar approach is discussed in the article [21], where a new phenomenological model is presented to demonstrate that it is capable of describing the influence of confinement on strength and displacement capacity, the presence of irreversible displacements, and the reduction of unloading stiffness, and the transition from tensile to compressive failure realistically.

The present study focuses on improving the numerical model of a prestressed beam to obtain the resulting values of stresses and vertical displacements that agree with the analytical solution. The parametric analyses considered the effect of varying the size of the finite element mesh, the strategy for creating differentiated mesh regions, how the introduction of prestressing force was simulated, and how its effect on the stress and strain state of the beam was determined. This research was carried out as a preliminary stage of a planned broader research program on prestressed concrete beams made of high-strength concrete. The concrete's compression and tension properties are described in this study by the CDP model, which is specifically designed to simulate the nonlinear behavior of concrete materials, particularly under various loading conditions. It effectively accounts for damage and plastic deformation in concrete structures, making it essential for accurate assessments.

2. ANALYTICAL MODEL

A rectangular beam with a 240 x 400 mm cross-section is supported over a 4600 mm span, as shown in Fig. 1. It is designed to carry a live point load of 28 kN in the middle of the span. The beam, made from concrete class C50/60, was initially designed to determine the optimum prestressing force and eccentricity of the rectangular cross-section with a straight tendon profile. The design was performed in

accordance with the specifications provided in Eurocode and fib Model Code [13, 14]. The used prestressing steel strand has a yield strength of 1660 MPa, an ultimate tensile strength of 1860 MPa, and an elastic modulus of 195000 MPa. All passive reinforcements, whether longitudinal or transverse, had a nominal tensile strength of 500 MPa. Figures 1 and 2 depict the beam's geometry and reinforcement details.
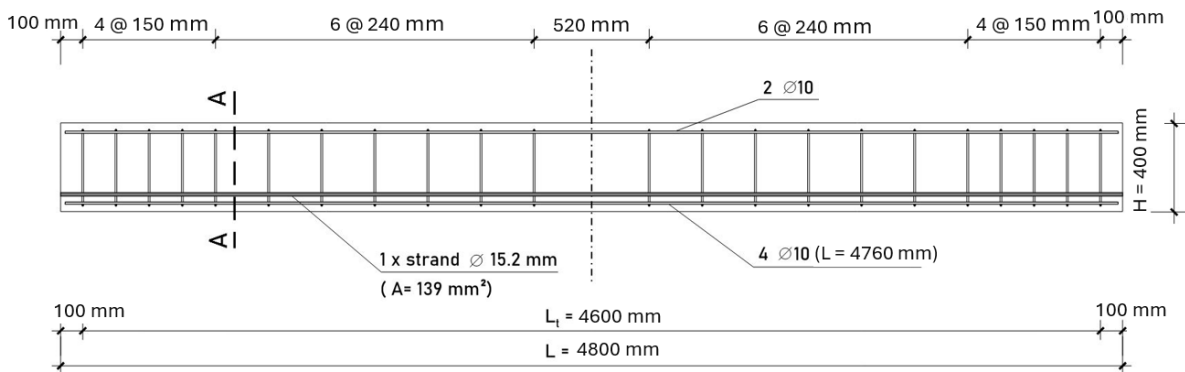

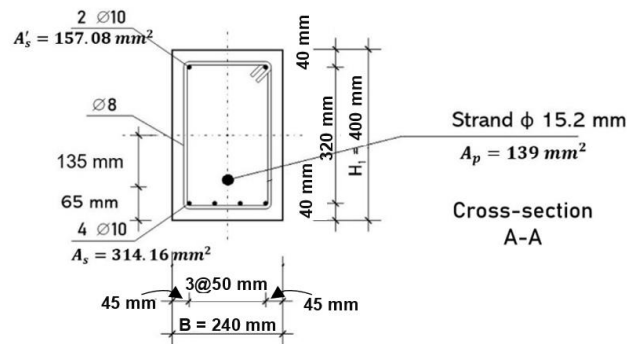Fig. 1. Reinforcement details of prestressed concrete beam

Fig. 2. The cross-section dimensions of the prestressed concrete beam at section A-A

Vertical forces are not exerted on the beam for a straight tendon profile. However, the ends of the beam are subject to a moment Pe, along with an axial force P, resulting in a diagram of the constant moment, as depicted in Fig. 3.

Fig. 3. Internal forces induced due to prestressing

Fig. 4 shows the stress distribution across the cross-section due to the prestressing force and external loading.
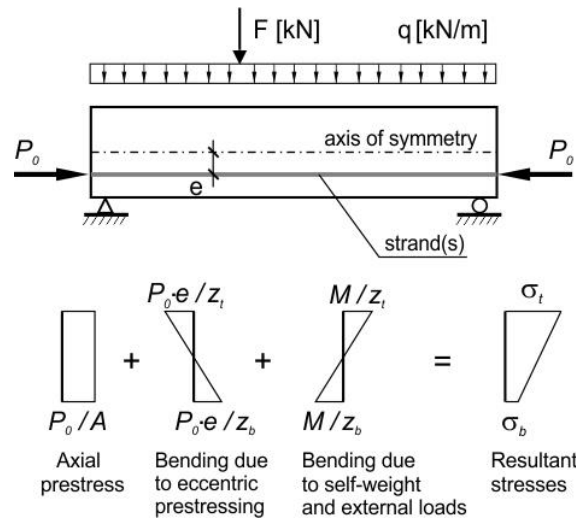

Fig. 4. Stresses in the beam with eccentric prestress force

The stresses at the outer fibers of the beam, given in Fig. 4, are calculated according to Eqns. (2.1) - (2.4):

Transfer stage

$$\sigma_t = \frac{P_o}{A_c} - \frac{P_o e}{Z_t} + \frac{M_{min}}{Z_t} \qquad (2.1)$$

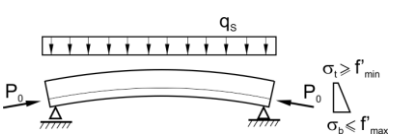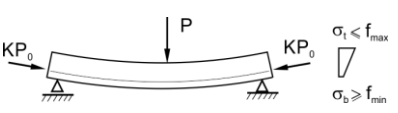$$\sigma_b = \frac{P_o}{A_c} + \frac{P_o e}{Z_b} - \frac{M_{min}}{Z_b} \qquad (2.2)$$

Service stage

$$\sigma_t = \frac{KP_o}{A_c} - \frac{KP_o e}{Z_t} + \frac{M_{max}}{Z_t} \qquad (2.3)$$

$$\sigma_b = \frac{KP_o}{A_c} + \frac{KP_o e}{Z_b} - \frac{M_{max}}{Z_b} \qquad (2.4)$$

in which P_o is the initial prestressing force, e is the eccentricity of straight tendon, A_c is the cross-section area of concrete, z_t and z_b are section moduli [$z_t = I/y_t$, $z_b = I/y_b$] (in mm³), I is the moment of inertia, and K is a factor that accounts for the prestress losses. For cross-sections without passive reinforcement, K is typically about 0.8 but may be significantly smaller for sections with passive reinforcement. M_{min} and M_{max} are bending moments due to the self-weight of the beam alone and self-weight plus external loads, respectively.

Numerous design approaches have been proposed to meet concrete stress limits, utilizing analytical and graphical techniques. The key to preventing cracking in prestressed members is to carefully select appropriate stress boundaries for both tensile stress of concrete at transfer (f'_{min}) and tensile stress under service load (f_{min}), as well as placing limits on concrete compressive stress at transfer (f'_{max}) and under-service loads (f_{max}). The following stress limits have been applied per the Eurocode standards used in this case study: $f'_{min} = 0.6\, f_{ctm}$ limiting tensile stress during transfer and

tension is not allowed under service load ($f_{min} = 0$), and imposing compressive stress limits at transfer $f'_{max} = 0.6\, f_{ck(t)}$, and at service $f_{max} = 0.6\, f_{ck}$. To ensure that the stress limits at transfer and under full loads are met, equations (2.5-2.8), as tabulated in Table 1, must be satisfied. In the case of a simply supported beam, the minimum moment at transfer and the maximum moment at service are governing the design, as illustrated in Figs. 5 and 6. These equations are then used to construct the four lines of the Magnel diagram in Fig. 7.

Table 1. Concrete stress limits for service ability limit state design

Deflection shapes at each loading stage		Stresses equilibrium equations	Magnel stress expressions
Transfer stage	Figure 5. Prestressed beam at transfer	$\dfrac{P_o}{A_c} - \dfrac{P_o e}{Z_t} + \dfrac{M_{min}}{Z_t} \geq f'_{min}$ (2.5)	$\dfrac{1}{P_o} \geq \dfrac{\left(\dfrac{1}{A_c} - \dfrac{e}{Z_t}\right)}{\left(f'_{min} - \dfrac{M_{min}}{Z_t}\right)}$
		$\dfrac{P_o}{A_c} + \dfrac{P_o e}{Z_b} - \dfrac{M_{min}}{Z_b} \leq f'_{max}$ (2.6)	$\dfrac{1}{P_o} \geq \dfrac{\left(\dfrac{1}{A_c} + \dfrac{e}{Z_b}\right)}{\left(f'_{max} + \dfrac{M_{min}}{Z_b}\right)}$
`Service stage	Figure 6. Prestressed beam at service	$\dfrac{KP_o}{A_c} - \dfrac{KP_o e}{Z_t} + \dfrac{M_{max}}{Z_t} \leq f_{max}$ (2.7)	$\dfrac{1}{P_o} \geq \dfrac{K\left(\dfrac{1}{A_c} - \dfrac{e}{Z_t}\right)}{\left(f_{max} - \dfrac{M_{max}}{Z_t}\right)}$
		$\dfrac{KP_o}{A_c} + \dfrac{KP_o e}{Z_b} - \dfrac{M_{max}}{Z_b} \geq f_{min}$ (2.8)	$\dfrac{1}{P_o} \leq \dfrac{K\left(\dfrac{1}{A_c} + \dfrac{e}{Z_b}\right)}{\left(f_{min} + \dfrac{M_{max}}{Z_b}\right)}$

The blue-shaded area in the Magnel diagram represents the safe combinations of prestressing force (P) and eccentricity (e) that ensure the concrete section can handle applied loads without exceeding the allowable stress limits for both tension and compression. For the most economical design, the ideal choice would be the uppermost point in this area, where $P_{max} = 123$ kN, as it minimizes the amount of prestressing steel required. However, this option is not feasible because it exceeds the maximum allowed eccentricity of ($e_{design} = 135\, mm$), which is a key constraint in the design. As a result, the design must use $P_o = 195\, kN$ at e = 135 mm, which remains within the safe zone, satisfies the eccentricity limit, and ensures the section remains structurally sound under all conditions. This approach balances safety requirements with practical design constraints while adhering to the permissible limits shown in the diagram.
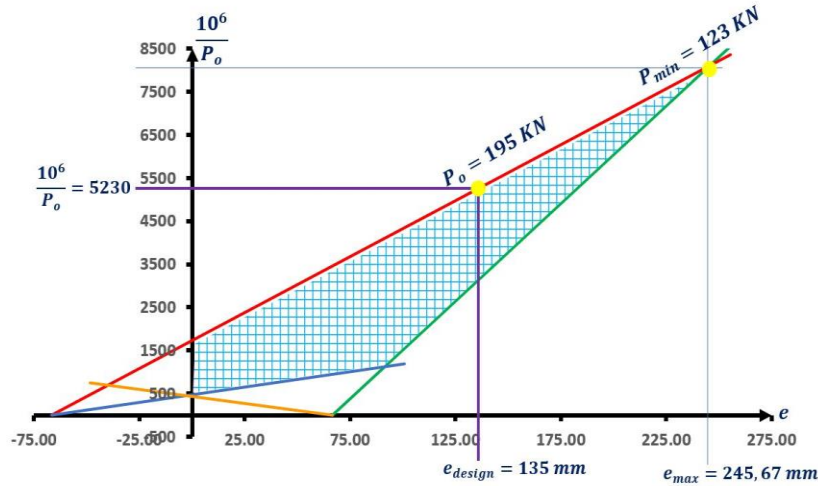
Fig. 7. Magnel diagram

The optimum values for the prestressing force and eccentricity at mid-span when neglecting any allowable tensile stress ($f_{min} = 0$) under the service load are 195 kN and 135 mm, respectively. These values are obtained using the equations in Table 1 in combination with the Magnel diagram in Fig. 7. In the analysis, stresses and deflections are calculated using the concept of the transformed section, and values of characteristic quantities of the cross-section are in Table 2.

The deflection Δ_p at transfer due to prestressing force P_o is,

$$\Delta_p = \frac{1}{8}\left(\frac{P_o(e-r)}{E_c\, I_{tr}}\right)L^2 \tag{2.9}$$

where L is the length of the beam, E_c is the elasticity modulus of concrete, I_{tr} is the moment of inertia for the transformed section, and r stands for the change in the neutral axis location ($r = \bar{y}_{tr} - \bar{y}$). To calculate the total displacement, the deflection due to prestressed force, self-weight, and live load should be added together.

Mid-span deflection at the transfer stage:

$$\Delta_T = \frac{1}{8}\left(\frac{P_o(e-r)}{E_c I_{tr}}\right)L^2 - \frac{5}{384}\left(\frac{w_s L^4}{E_c I_{tr}}\right) \tag{2.10}$$

Mid-span deflection at the service stage:

$$\Delta_S = \frac{1}{8}\left(\frac{P_o(e-r)}{E_c I_{tr}}\right)L^2 - \frac{5}{384}\left(\frac{w_s L^4}{E_c I_{tr}}\right) - \frac{1}{48}\left(\frac{PL^3}{E_c I_{tr}}\right) \tag{2.11}$$

where w_s is the self-weight of the beam, and P is the live load. The transformed area (A_{tr}) is calculated as

$$A_{tr} = A_c + (n_p - 1)A_p + (n_s - 1)A_s + (n_s - 1)A'_s \tag{2.12}$$

with A_s being the cross-sectional area of the bottom rebars, A'_s – the cross-sectional area of the top rebars and $n_p = E_p/E_c$ and $n_s = E_s/E_c$ are the ratio of the elasticity modulus of strands and rebars to the

elasticity modulus of concrete, respectively. Then, the transformed moment of inertia is calculated as follows,

$$I_{tr} = I + \sum_{i=1}^{m} A_{(i)} \times d_i^2 \tag{2.13}$$

where m is the number of areas; in this case, there are four different types of areas (see Eq. (2.12)), and d_i is the distance from the centre of each area to the outer fiber. Table 2 gathers the values obtained from the analytical solution. The stresses along the height of the beam $(\sigma_{33})_{tr}$ for the transformed section are recalculated from equations (2.4) to (2.8).

Table 2. Properties of the transformed section

Parameters	Active reinforcement only	Passive & active reinforcement
A_{tr} (cm^2)	965.9	986.7
y_{tr} (cm)	200.8	201.9
I_{tr} (cm^4)	129075.1	134356.7

3. COMPUTATIONAL MODEL

When performing a finite element analysis of a prestressed concrete beam using Abaqus, various aspects must be considered. These include geometry, boundary conditions, material properties, meshing, and interpretation of the numerical results.

3.1 Model geometry

The model's geometry, including the concrete beam, strands, other reinforcements, and supports, as shown in Figs. 1, 2, and 8, was created in ABAQUS/CAE. Geometrical aspects, materials, boundary conditions, and interactions were defined at the initial stage. The concrete section was created using an 8-node 3D solid linear brick with reduced integration (C3D8R) and (C3D8I). Steel reinforcement, stirrups, and prestressing tendons were modelled using a 2-node linear 3D truss element (T3D2) as described in references [22,23,24,25]. All reinforcements were fully bonded with the concrete using embedded technology, which defined concrete as the host material. As a result, rebar elements could only have translations or rotations with a degree of freedom equal to those of the host elements surrounding them [26]. Selecting the appropriate solid element is crucial for accurately determining deflections and stresses in Abaqus. Abaqus provides several common element types, including C3D8, C3D8I, and C3D8R. However, each type of element has its characteristics, advantages, and limitations that can affect the accuracy of the results. The C3D8 element, for instance, is a general-purpose linear brick element that is fully integrated with eight integration points. The C3D8 element is well-suited for general-purpose structural analyses, including beam bending problems. However, it is too stiff to bend, so we need to refine the mesh to achieve accurate results. The C3D8I element is an advanced version of the C3D8 eight-node brick element, designed to provide superior accuracy in solving problems with bending and shear deformations. Regarding beam bending analyses, the C3D8I element is an excellent choice for obtaining precise deflection and local stresses. On the other hand, the C3D8R element is a linear brick element that uses only one integration point, making it a more versatile option, and it has an advantage over other types when it comes to detecting damages specified in the CDP model. However, it may not be stiff enough for problems involving bending. The stresses and strains are most accurate in the middle of the element where the integration point is located. Therefore, small elements are necessary to capture stress concentration at the boundary of a structure [27].
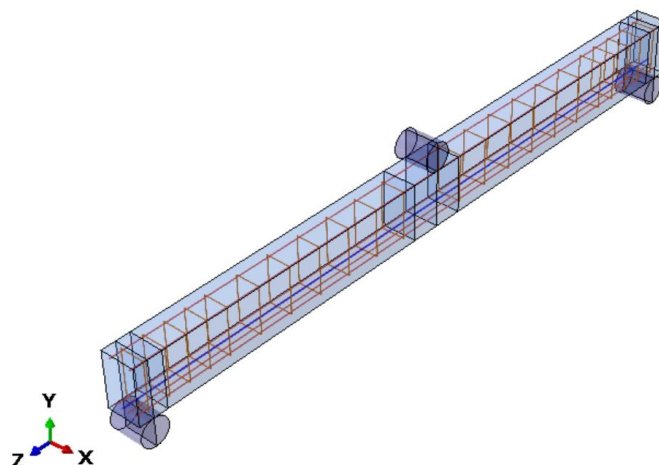
Fig. 8. Finite Element Model of the prestressed beam

3.2 Loads and boundary conditions

Abaqus provides various boundary condition options to replicate different scenarios, such as fixed support, pinned support, and displacement constraints. Properly setting up boundary conditions is crucial to simulate the realistic behaviour of the beam precisely. In this study, the ends of the span are pinned. U1 and U2 are set to zero to prevent out-of-plane displacement in the X-direction or fall vertically in the Y-direction; in order to obtain symmetrical deflection, U3 (Z-direction) was set to zero at mid-span. The load was applied using coupling constraints of the type of structural distribution. It is essential to define reference points linked to the loading object and support in the history output. This will help obtain the complete historical outputs of reaction forces, applied load, and displacements, which can be used later for validation purposes and drawing a force-to-displacement diagram. The loads are applied in two stages. In the first stage, self-weight, which was defined as the beam's gravitational load, and the prestressing force were applied. In the second stage, the beam was first loaded by a design load of 28 kN and then loaded to failure.

3.3 Interaction

This study strongly recommends a careful definition of the interaction conditions because they not only affect the accuracy of the analysis but also highly affect the convergence of the simulation and analysis time. The interaction between the steel reinforcement and strand with the concrete was defined using embedded technology; this feature in Abaqus allows us to model all types of reinforcements as truss elements, which saves time by reducing the number of elements compared to solid elements, improves the chance of converging, and reduces computational efforts. Another essential aspect that should be defined in this section is the contact behaviour of the supports. In this study, hard contact property is defined, and separation was allowed after the contact, which is significant for PSC beams due to the axial force caused by prestressing. Since the friction property is not considered in the analytical solution; thus, we assumed frictionless behaviour at the supports.

3.4 Methods of Applying Prestressing Force

Two methods were employed for introducing pretension in strands:

i) The first method involved applying initial stress, and the applied stress was determined using Eq. (3.1), further denoted as AIS models:

$$\sigma_p = \frac{P_o}{A_p} = \frac{195\ \text{kN}}{139\ \text{mm}^2} = 1402.8\ \text{MPa} \tag{3.1}$$

ii) The second method used the idea of cooling, further denoted as BT models. The magnitude of the applied negative temperature utilized in the cooling method is determined using Eq. (3.2) [9, 24],

$$\Delta T = -\frac{P_o}{\alpha\ E_p\ A_p} \tag{3.2}$$

where α is the coefficient of thermal expansion ($\alpha = 1.2 \times 10^{-5}/°\text{C}$), E_p and A_p are the strand's modulus of elasticity and the cross-sectional area of the strand, respectively. In the considered case, we have $\Delta T = -599.5\ °\text{C}$.

The value of σ_p should be smaller or equal to $\sigma_{p,max}$, $\sigma_p \leq \sigma_{p,max}$, and $P_o \leq P_{max}$. Where σ_p and P_o are the initial stress and initial prestressing force in the strand, respectively. EN 1992-1-1 [13] defines the mean prestressing force at any time (t) and at a certain distance (x) from the active ends of a strand as $P_{m,t}(x)$. This force is equal to the maximum force P_o also called jacking force P_j which is applied at the active end of the tendon during tensioning, minus the immediate and time-dependent losses. The initial force P_o must satisfy:

$$P_o \leq A_p \sigma_{p,max} \tag{3.3}$$

where

$\sigma_{\text{p.max}}$ is the smaller of $\begin{cases} 80\% \text{ of the characteristic tensile strength (i. e. } 0.8\ f_{pk}) \\ 90\% \text{ of the characteristic } 0.1\% \text{ proof stress (i. e. } 0.9\ f_{p0.1k}) \end{cases}$

3.5 Modelling of Materials

An accurate representation of the material behaviour in its computational simulation by the finite element method is crucial to obtain reliable results. Abaqus is sophisticated software that offers various models to define material behaviour, including isotropic, orthotropic, and anisotropic properties. Moreover, Abaqus provides a broad range of material models to simulate the behaviour of different materials, such as steel, concrete, and composite materials [6, 27]. The material models that we used for the prestressed concrete beam are described.

3.5.1 Concrete

In this study, a Concrete Damage Plasticity (CDP) model was used for concrete, whose characteristic strain-stress relationships for tension and compression are shown in Fig.9. The CDP implemented in Abaqus is based on the seminal works of Lubliner et al. [17] and Lee & Fenves [18], and modified version of the Drucker-Prager strength hypothesis [28]. Lubliner et al. [17] developed a constitutive model for the nonlinear analysis of concrete that takes into account the effects of stiffness degradation and strain softening in both compression and tension. These factors lead to a more accurate representation of the behaviour of concrete structures under various loads. Szczecina and Winnicki performed numerical simulations on a concrete specimen using the CDP model in Abaqus for biaxial compression and uniaxial tension tests [29]. The authors recommended that the viscosity parameter

should be taken equal to 0.0001 and the dilation angle 5 degrees. Hafezolghorani *et al.* proposed a simplified model for an unconfined prestressed concrete beam. A simplified concrete damage plasticity (SCDP) model was created by merging a stress-based plasticity component with a strain-based damage model [30]. In a paper [31], Hasan and Darbaz conducted a comparative study of commonly used CDP material parameters. Like the previous authors, it was once again emphasized that in selecting the various parameters of the CDP model, one must do so very carefully, depending on the specifics of the test under consideration.
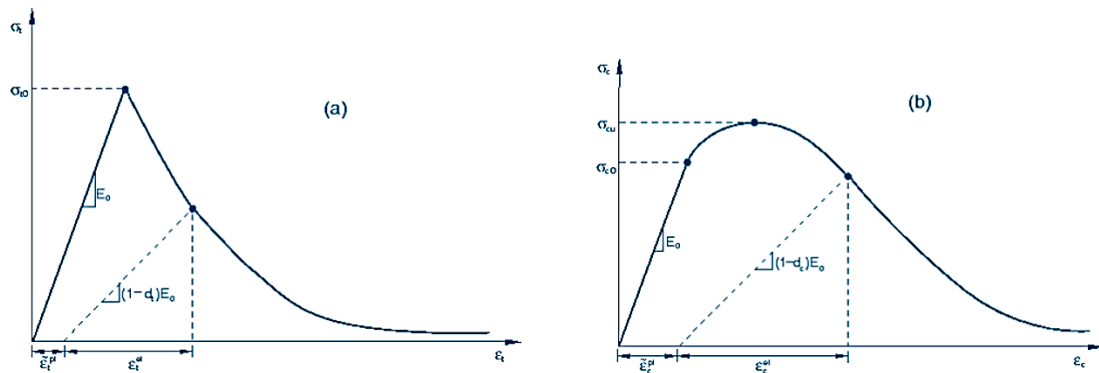

Fig. 9. Response of concrete to uniaxial loading in tension (a) and compression (b) [6, Abaqus]

The total strain tensor ε, in the softening branch of stress-strain curves for the compression and tension regimes, see Fig. 9, can be additively split into an elastic part ε_0^{el} and an inelastic part, $\tilde{\varepsilon}^{in}$, or into a part with damaged elastic stiffness, ε^{el}, and an equivalent plastic part, $\tilde{\varepsilon}^{pl}$, which can be defined as follows

$$\varepsilon = \varepsilon_0^{el} + \tilde{\varepsilon}^{in} = \varepsilon^{el} + \tilde{\varepsilon}^{pl} \tag{3.4}$$

$$\varepsilon_0^{el} = \frac{\sigma}{E_0}, \qquad \varepsilon^{el} = \frac{\sigma}{(1-d)E_0} \tag{3.5}$$

$$\tilde{\varepsilon}^{in} = \varepsilon - \varepsilon_0^{el} \tag{3.6}$$

$$\tilde{\varepsilon}^{pl} = \varepsilon - \varepsilon^{el} \tag{3.7}$$

where E_0 is the modulus of elasticity of initial (undamaged) material, and d is a damage parameter being a scalar measure of the degradation of material stiffness, with $0 \leq d \leq 1$, and the meaning of limit values: $d = 0$ – undamaged material, $d = 1$ – fully damaged material. The stress-strain relationships under uniaxial tension, $\sigma_t - \varepsilon_t$, and compression, $\sigma_c - \varepsilon_c$, loading is expressed as

$$\sigma_t = (1-d_t)E_0(\varepsilon_t - \tilde{\varepsilon}_t^{pl}) \tag{3.8}$$

$$\sigma_c = (1-d_c)E_0(\varepsilon_c - \tilde{\varepsilon}_c^{pl}) \tag{3.9}$$

with ε_t and ε_c denoting the total tensile and compressive strains, respectively, and the plastic strains

$$\tilde{\varepsilon}_t^{pl} = \tilde{\varepsilon}_t^{ck} - \left(\frac{d_t}{1-d_t}\right)\varepsilon_{t,0}^{el} \tag{3.10}$$

$$\tilde{\varepsilon}_c^{pl} = \tilde{\varepsilon}_c^{in} - \left(\frac{d_c}{1 - d_c}\right)\varepsilon_{c,0}^{el} \tag{3.11}$$

where $\tilde{\varepsilon}_t^{ck}$ is a cracking strain at tension, d_t and d_c are the tension and compression damage variables, with $0 \leq d_t \leq 1$ and $0 \leq d_c \leq 1$,

$$d_t = 1 - \frac{\sigma}{\sigma_{t0}} \tag{3.12}$$

$$d_c = 1 - \frac{\sigma}{\sigma_{cu}} \tag{3.13}$$

The plastic strain is calculated also to ensure that it is positive. A negative value of plastic strain (both in compression or tension) would cause convergence issues in the analysis and may result in an error and termination of the job in Abaqus. Tables 3 and 4 contain numerical values of the data defining the inelastic behaviour of the concrete in compression and in tension, which we used in the CDP model implemented in the Abaqus program.

Table 3. Concrete elastic and plastic properties for the CDP model

Material parameters	C50/60	Plasticity Parameters	
		Dilation angle	30
Concrete Elasticity		Eccentricity	0.1
		fb_0/fc_0	1.16
Elasticity Modulus	37000 MPa	K	0.667
Poison ratio	0.2	Viscosity parameter	0.001

Table 4. Inelastic compressive & tensile behaviour data for the CDP model

Inelastic compressive concrete behaviour with damage			Inelastic tensile concrete behaviour with damage		
Yield stress (MPa)	Inelastic strain	Damage d_c	Yield stress (MPa)	Cracking strain	Damage d_t
22.422	0.0	0	4.100	0.0	0
27.302	0.000012	0	0.050	0.0015	0.990
31.834	0.000040	0			
35.981	0.000078	0			
39.701	0.000127	0			
42.948	0.000189	0			
45.666	0.000266	0			
47.791	0.000358	0			
49.248	0.000469	0			
50.000	0.000600	0			
49.795	0.000754	0.003			
48.656	0.000935	0.026			
46.387	0.001146	0.071			
42.807	0.001393	0.143			
37.696	0.001681	0.245			
30.780	0.002018	0.384			
21.719	0.002413	0.565			
18.679	0.002545	0.626			
8.620	0.003134	0.827			

Extensions of the above relations of the CDP model to a general 3D stress state are defined by the two main elements, the stress-strain relationships

$$\boldsymbol{\sigma} = (1 - d)\boldsymbol{E}_0 : (\boldsymbol{\varepsilon} - \boldsymbol{\varepsilon}^{pl}) \tag{3.14}$$

in which the elastic material stiffness $\boldsymbol{E}_0$ is reduced by the scalar damage parameter d, $\boldsymbol{\varepsilon}$ is the total strain tensor, and $\boldsymbol{\varepsilon}^{pl}$ is the tensor of plastic strains whose evolution is governed by the flow rule $\dot{\boldsymbol{\varepsilon}}^{pl} = \dot{\lambda}\boldsymbol{g}$, where $\dot{\lambda} \geq 0$ is the plastic loading multiplier, and $\boldsymbol{g} = \partial G/\partial\boldsymbol{\sigma}$ is the plastic flow vector that is normal to the plastic potential function G. (2) the Kuhn–Tucker complementarity conditions (loading/ unloading conditions), which govern the evolution of the elasto-damage-plastic deformation process with damage

$$F \leq 0, \quad \dot{\lambda} \geq 0, \quad F\dot{\lambda} = 0 \tag{3.15}$$

wherein F is the yield function, or other function definig a scalar threshold value for an irreversible process. We remark that also the rate of the damage variables should not be negative, i.e. $\dot{d}_t \geq 0$, $\dot{d}_c \geq 0$. For further details, the reader may consult references [27, 17, 18, 32, 33].

3.5.2 Steels

The one-dimensional bilinear elastoplastic behaviour and assumption of a perfect bond between steel and concrete are used to model rebars and stirrups and their interaction with the concrete. The same approach was taken for the strands, considering a 7-wire strand. The properties of the strand and other reinforcements are tabulated in Tables 5 and 6.

Table 5. Properties of the prestressed strands of type Y1860S7

Nominal diameter (mm)	Cross-sectional area-A_p (mm^2)	Characteristic breaking force (kN)	Max. breaking force (kN)	Yield force at 0.1% proof strain (kN)	Number of strands
15.2	139	258.5	297.3	223	1

Table 6. Material properties of structural reinforcements

Material	Diameter (mm)	Yield stress (MPa)	Ultimate tensile strength (MPa)	Elasticity modulus (GPa)
Strand	15.2	1660	1860	195
Longitudinal steel	10	500	575	200
Stirrups	8	500	575	200

4. REFINEMENT AND VERIFICATION OF THE FEA MODEL

The accuracy and reliability of the FEA models were optimized and verified against the analytical solution through two phases to ensure that the numerical analysis aligns with the analytical solution. Specific parameters were adjusted, and other parameters were changed to minimize differences between numerical and analytical results. Ten computational models were developed; nine were reinforced solely with active reinforcement (strands only), and model AP-M18-06 has both active reinforcements and passive (longitudinal rebars and stirrups).

4.1 Phase One: Mesh Refinement and Prestressing Techniques

Two prestressing methods were examined. To reduce the simulation time, all the models in this phase were reinforced solely with active reinforcement. In addition, the analysis in this phase focuses on the transfer stage only, as we believe precisely predicting a beam's behaviour during the elastic stage provides a strong foundation for anticipating its performance during the inelastic stage. This understanding is essential for more reliable and effective simulations at an advanced level. Two sets of models were developed based on their prestressing techniques, as outlined in Table 7. Each set comprises three models with three different mesh sizes, and the two sets are classified by their prestressing techniques. Models in set A utilized predefined stress (initial stress), whereas models in set B employed predefined temperature (cooling). As emphasized in references [34, 35, 36], conducting a mesh sensitivity analysis is indispensable in the realm of prestressed concrete structures due to their complex behavior. Therefore, it is imperative to ensure that the mesh is sufficiently refined to capture local effects accurately, specifically local stresses and deflection. To this end, three additional models with varying mesh sizes and strategies were examined. Table 8 provides specific details on the meshing strategies of these models based on the segmentation shown in Fig. 10. The primary goal of this phase was to compare the two methods for introducing prestressing force in ABAQUS and identify the optimal mesh size that balances computational efficiency and accuracy for reliable numerical simulations. Therefore, the optimal model was identified for further analysis in the subsequent phase following the inclusion of passive reinforcement. The maximum element sizes in these models were 25 mm, 20 mm, 18 mm, 15 mm, 14 mm, and 11 mm.

Table 7. Models with different mesh sizes, set (A) and (B)

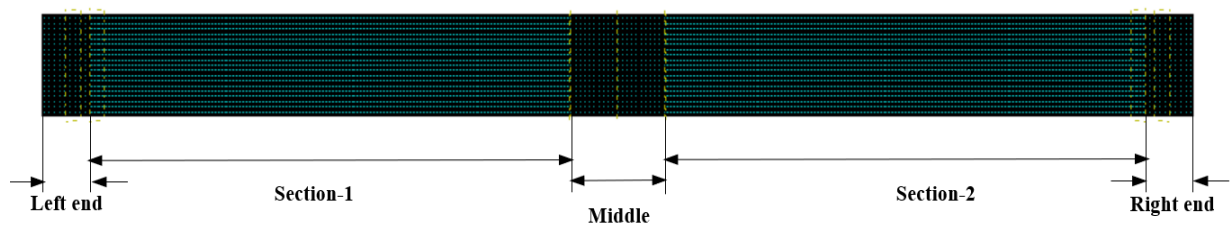| Models set (A)	Mesh size of concrete (mm)	Mesh size of the strand (mm)	Models set (B)	Mesh size of concrete section (mm)	Mesh size of the strand (mm)
AIS-M25	25	10	BT-M25	25	10
AIS-M20	20	10	BT-M20	20	10
AIS-M15	15	10	BT-M15	15	10

Fig. 10. Sections with different mesh sizes for models in Table 8

Table 8. Models with different mesh sizes

Models (set B)	Mesh size of concrete sections (mm)					Mesh size of the strand (mm)
	Left end	Section-1	Middle	Section-2	Right end	
BT-M11-08	8	11	8	11	8	5
BT-M14-10	10	14	10	14	10	5
BT-M18-06	6	18	6	18	6	5

4.2 Phase two: passive reinforcement added

In this phase, a new model, AP-M18-06, was developed. It is similar to BT-M18-06 in phase one but with an additional feature of passive reinforcement (longitudinal rebars and stirrups). The type of element at the middle section of concrete right below the loading point also changed from C3D8R to C3D8I to better capture local stresses. This phase was conducted in two stages: the transfer stage and the service stage.

i)   In the transfer stage, only gravity and prestressing forces were included, and the beam was hogged up, Fig.13 (a).
ii) The service stage is a continuity of the transfer stage, where the beam was loaded at mid-span Fig. 13 (b) to examine the load-bearing capacity of the prestressed beam under service loads.

5. RESULTS AND DISCUSSION

The comparison with analytical solutions serves as a significant verification of the numerical approach, thereby enhancing confidence in the accuracy of the finite element analysis. This study investigated the influence of the prestressing methods and mesh sizes on the deflection and stresses by varying the prestressing methods, meshing sizes, and types of elements. The outcomes revealed that finer meshes and element type C3D8I captured localized effects, which resulted in more accurate mid-span deflection and stress distribution. In contrast, coarser meshes neglected important details, which ultimately affected the results. Furthermore, the choice of meshing strategy, types of elements, interaction property, and boundary conditions used in this study had critical effects on shortening simulation times, convergence of the numerical analysis, and accuracy of the results. Tables 9 and 10 present the verification results of the numerical model, along with the percentage errors for phase one and phase two, respectively.

5.1 Analytical and numerical results for phases one

All the models in this section are solely reinforced with strands and cover only the transfer stage. Upon careful examination, it was evident that model BT-M18-06 outperforms all other models in phase one and displayed superior results across other models. The stress along the height of the beam (σ_{33}) in Figure 12 and the analytical results in Table 9 are perfect matches. Additionally, its deflection percentage error was only 1.029% (0.012mm). Moreover, the percentage errors of the top and bottom stresses were 1,158% and 0.428%, respectively. The percentage errors of deflection and stresses are calculated at each stage separately based on Eqns. (5.1) and (5.2).

$$\Delta^e \ (\%) = \frac{\Delta_{ant} - \Delta_{num}}{\Delta_{ant}} \times 100 \tag{5.1}$$

$$\sigma^e \ (\%) = \frac{\sigma_{ant} - \sigma_{num}}{\sigma_{ant}} \times 100 \qquad (5.2)$$

where, Δ^e is the percentage error of deflection, Δ_{ant} is analytical deflection and Δ_{num}, is numerical deflection. σ^e is the percentage error of stresses, σ_{ant} and σ_{num} are the analytical and numerical stresses at the mid-span of the beam, respectively.

Table 9. Deflection and normal stresses at the mid-span - Analytical solution vs numerical results – phase one

Models	Prestressing Methods	Deflection (mm)		Stresses (MPa)			
		Δ	Δ^e (%)	Top surface stress (σ_t)	σ_t^e (%)	Bottom surface stress (σ_b)	σ_b^e (%)
Analytical Solution	-	1.166	-	-1.123	-	5.135	-
AIS-M25	Initial S	0.9051	22.376	-1.04	7.391	5.041	1.831
AIS-M20	Initial S	0.9996	14.271	-1.055	6.055	5.056	1.538
AIS-M15	Initial S	1.083	7.118	-1.069	4.809	5.076	1.149
BT-M25	Cooling	0.9061	22.290	-1.042	7.213	5.045	1.753
BT-M20	Cooling	1.001	14.151	-1.056	5.966	5.061	1.441
BT-M15	Cooling	1.084	7.033	-1.070	4.72	5.077	1.130
BT-M11-08	Cooling	1.140	1.893	-1.097	2.315	5.08	1.071
BT-M14-10	Cooling	1.127	3.012	-1.085	3.384	5.089	0.896
BT-M18-06	Cooling	1.154	1.029	-1.110	1.158	5.113	0.428

Δ is the deflection, σ_t and σ_b are the top and bottom stresses taken at the mid-span of the beam, respectively. σ_t^e and σ_b^e are the percentage errors of top stress (tensile) and bottom stress (compressive) at the mid-span, respectively.
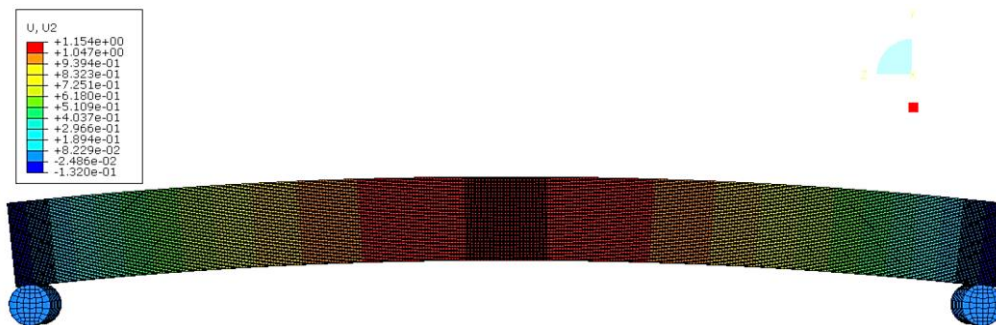

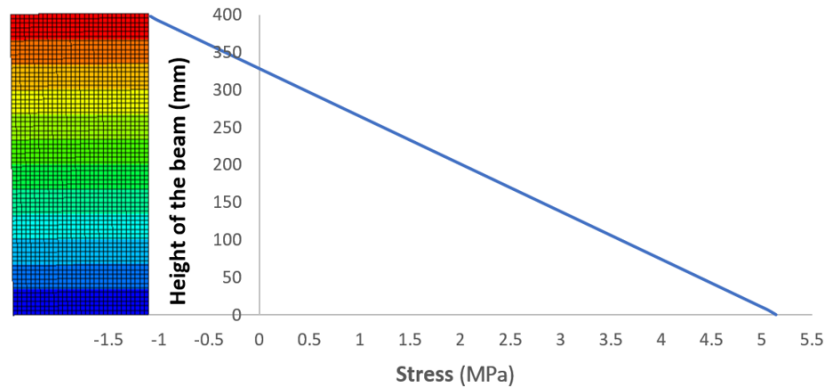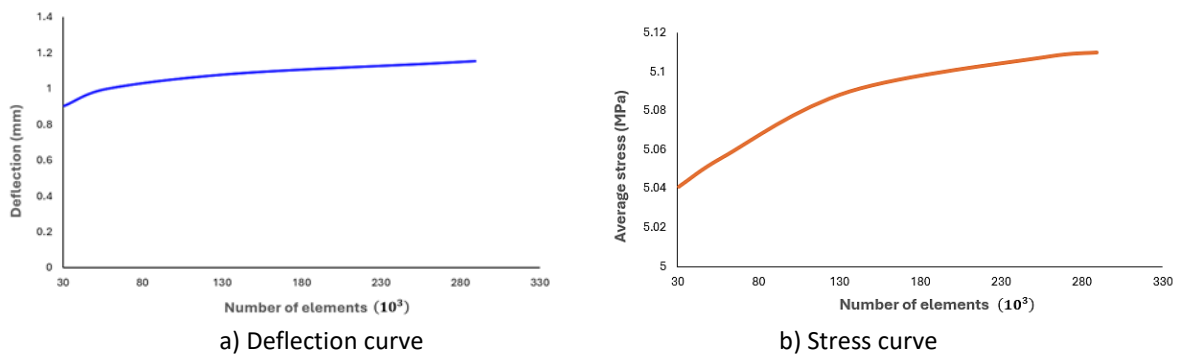Fig. 11. Deflection of the beam at Transfer Stage-Model BT-M18-06

Fig. 12. Normal stresses (σ_{33}) **-** Transfer Stage-Model BT-M18-06

a) Deflection curve   b) Stress curve

Fig. 13. Mesh convergence curves for deflection and stress at the mid-span

5.2 Analytical and numerical results for phase two - model AP-M18-06

5.2.1   Elastic range

The results presented in this section are for model AP-M18-06. As expected, achieving positive results in the simplified models from phase one will lead to positive outcomes in more complex models. During the transfer stage, the model showed a deflection percentage error of only 0.274%, equivalent to just 0.003 mm. Meanwhile, the tensile stress at the top was -1.011 MPa with a percentage error of 0.785%, and compressive stress at the bottom was 4.906 MPa with a percentage error of 0.183% as in Table 10 and Figure 14. a. The maximum tensile stress at the top of the beam during the transfer stages was only 25% of the characteristic tensile strength ($f_{ctm} = 4.1$ MPa), for class 50/60, which falls within the allowed range.

5.2.2   Design for service load of 28 kN within the elastic range

The beam was designed to withstand a point load of 28 kN at the mid-span without experiencing any tensile stresses. The results showed that the beam was fully compressed at the applied load. The stress at the top was 4.010 MPa with a percentage error of 4.974%, while the stress at the bottom was 0.1663 MPa with a percentage error of 1.012%, as shown in Table 10 and Figure 14.b.

Table 10. Comparison of analytical solution and numerical results of Model AP-M18-06

Computational Methods	Loading stages	Deflection (mm)		Stresses (MPa)			
		Δ	Δ^e (%)	top stress (σ_t)	σ_t^e (%)	bottom stress (σ_b)	σ_b^e (%)
Analytical Solution	Transfer stage	1.096	-	-1.019	-	4.915	-
	Service stage	-0.039	-	3.820	-	0.188	-
Numerical Results AP-M18-06	Transfer stage	1.093	0.274	-1.011	0.785	4.906	0.183
	Service stage	-0.038	2.564	4.010	-4.974	0.166	1.012

a)   Transfer stage
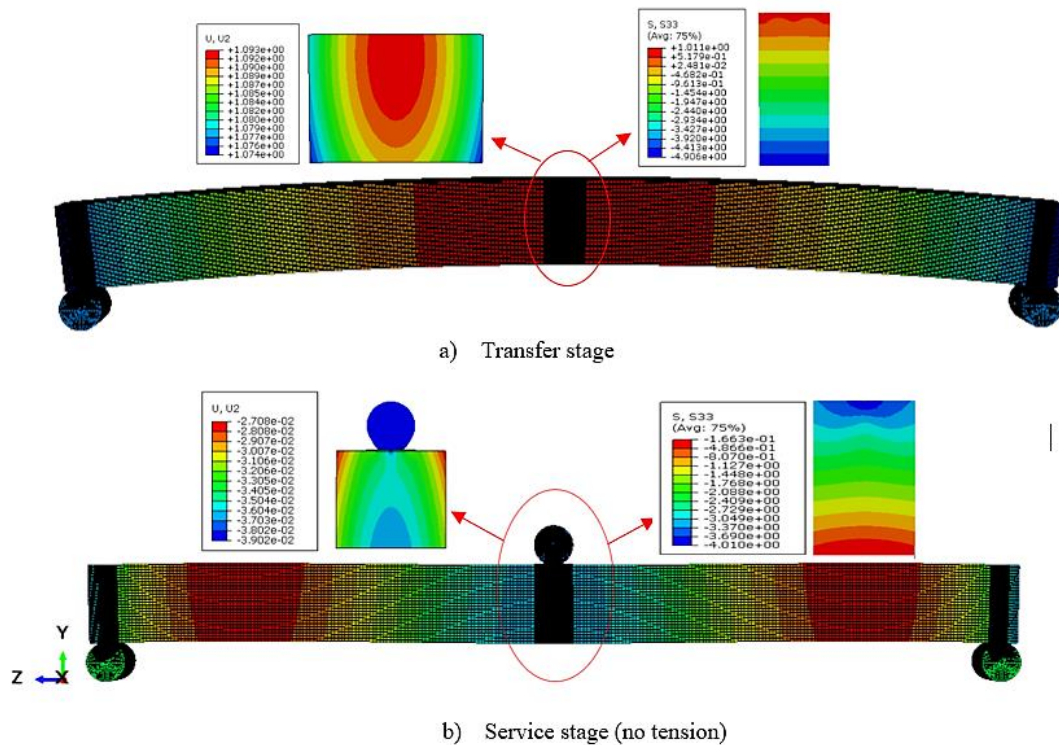

b)   Service stage (no tension)

Fig. 14. Deflection of a beam – Model AP-M18-06

5.2.3   Inelastic range (The nonlinear behaviour)

The beam was loaded to the failure, and the first sign of damage occurred at the bottom surface of the mid-span at $\sigma_{33} = 4.106$ MPa, which corresponds to the tensile yield stress of concrete defined in the CDP model Table 4. The force required to initiate the first crack was $P_{cr} = 53.121$ kN with a percentage error of only 0.148% in comparison to the analytical solution, and the first sign of nonlinearity began when the tensile damage parameter in concrete reached $d_t = 0.99$, marked as point (C) in Figures 15 and 16, also check Fig17.c, and this occurred at $P = 66.076$ kN. The results of this section are graphically summarized in Figures 15 through 17.

The force-deflection curve in Figure 15 highlights the beam's behaviour under increasing loads. Initially, the curve shows a linear elastic response from point (A) to the first cracking point (B). Beyond this, the beam reaches a yield point (C), where plastic deformation begins, resulting in a nonlinear

response; the curve rises until the ultimate strength of the strand point (2) and then to the ultimate compressive strength at point (D). The curve then shows a gradual increase in deflection with a decrease in force; then, the failure occurs at point (E). On the other hand, point (1) represents the yield strength of the strand.

The beam exhibited good stiffness in the linear region, characterized by a steep slope on the force-deflection curve. Additionally, it displayed ductile behaviour by allowing significant deflection before failure, indicating a degree of structural robustness. Upon comparing the numerical results with analytical solutions, we observed significant agreement in the linear region but slight discrepancies in the nonlinear range. These differences may be attributed to assumptions made in the numerical model or material properties not fully captured in the analysis. By providing a thorough explanation of these points, we have gained a comprehensive understanding of how the beam behaves under loading conditions and can draw valuable insights for further analysis and design considerations.

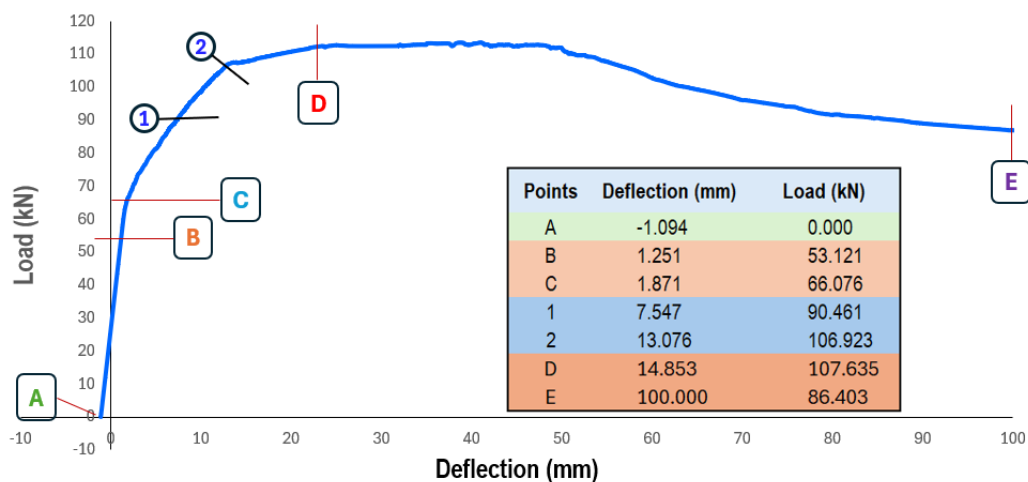| Points	Deflection (mm)	Load (kN)
A	-1.094	0.000
B	1.251	53.121
C	1.871	66.076
1	7.547	90.461
2	13.076	106.923
D	14.853	107.635
E	100.000	86.403

Fig. 15. Force versus displacement – Model AP-M18-06

Figure 16 illustrates the stress distribution along the height of beam AP-M18-06 at mid-span during various loading stages, from prestress transfer to ultimate failure. Initially, compressive stresses dominate at the transfer stage (A), followed by the appearance of tensile stress at the bottom of the beam at first crack (B) and progressing to full tension damage $d_t = 0.99$ at (C). At the ultimate compressive strength of concrete (D), the top region experiences maximum compression, while the bottom is critically cracked. Finally, at failure (E), the beam undergoes structural collapse, marked by extensive cracking and stress redistribution. The stress contours visually represent these transitions. Figure 17 complements this by visualizing the crack progression using DAMAGET contours. Minor damage is concentrated at the bottom mid-span of the beam at the first cracking load. As the load increases, this damage propagates upward and outward, and extensive crack propagation throughout the beam indicates severe structural damage and an imminent collapse (Fig17.d). Together, these figures provide a comprehensive understanding of the beam's behaviour under increasing loads.
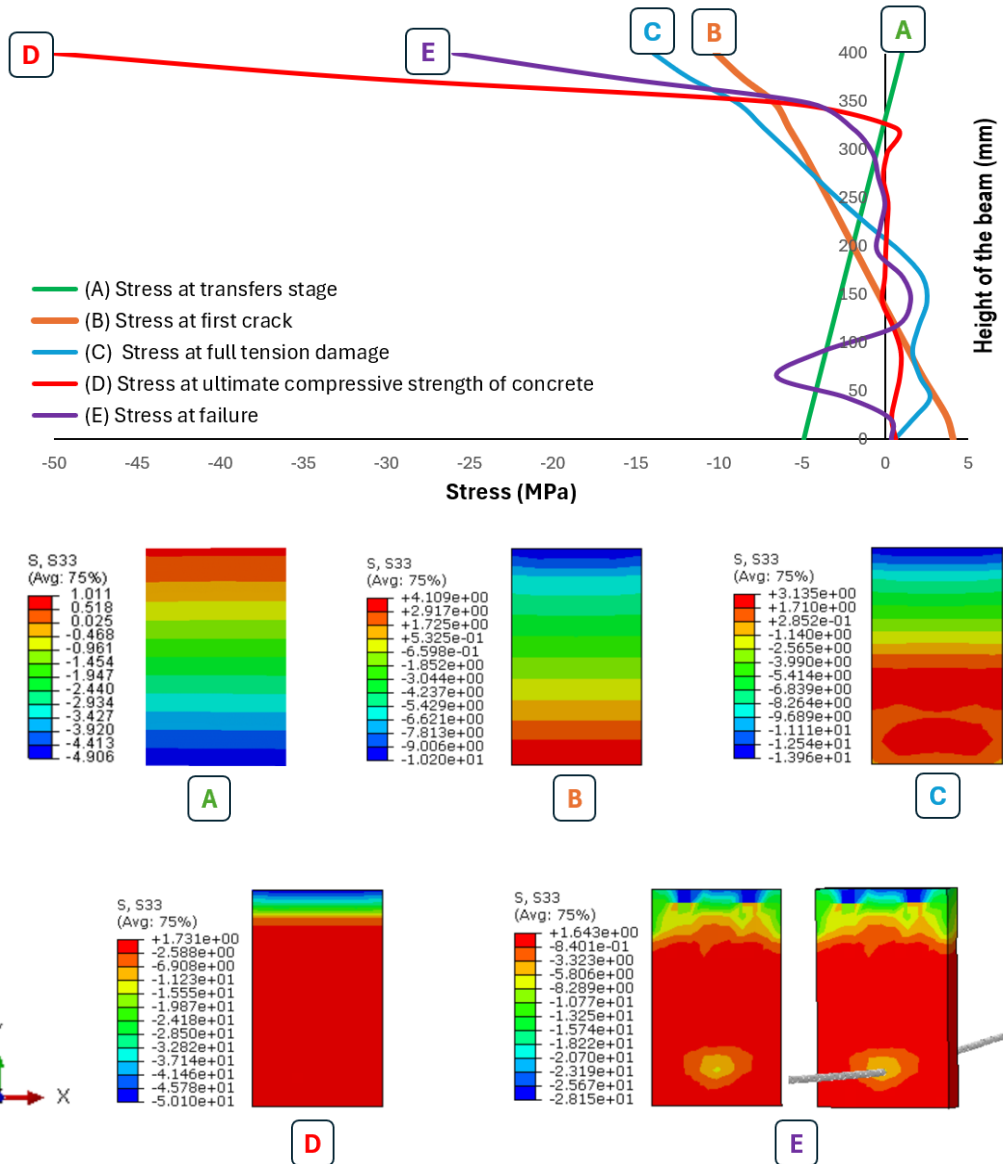
Fig. 16.Stress along the height of the beam at mid-span at different loading stages – Model AP-M18-06

Notation: the digits preceding e+01 should be multiplied by 10, and the digits preceding e-01 should be divided by 10, etc.
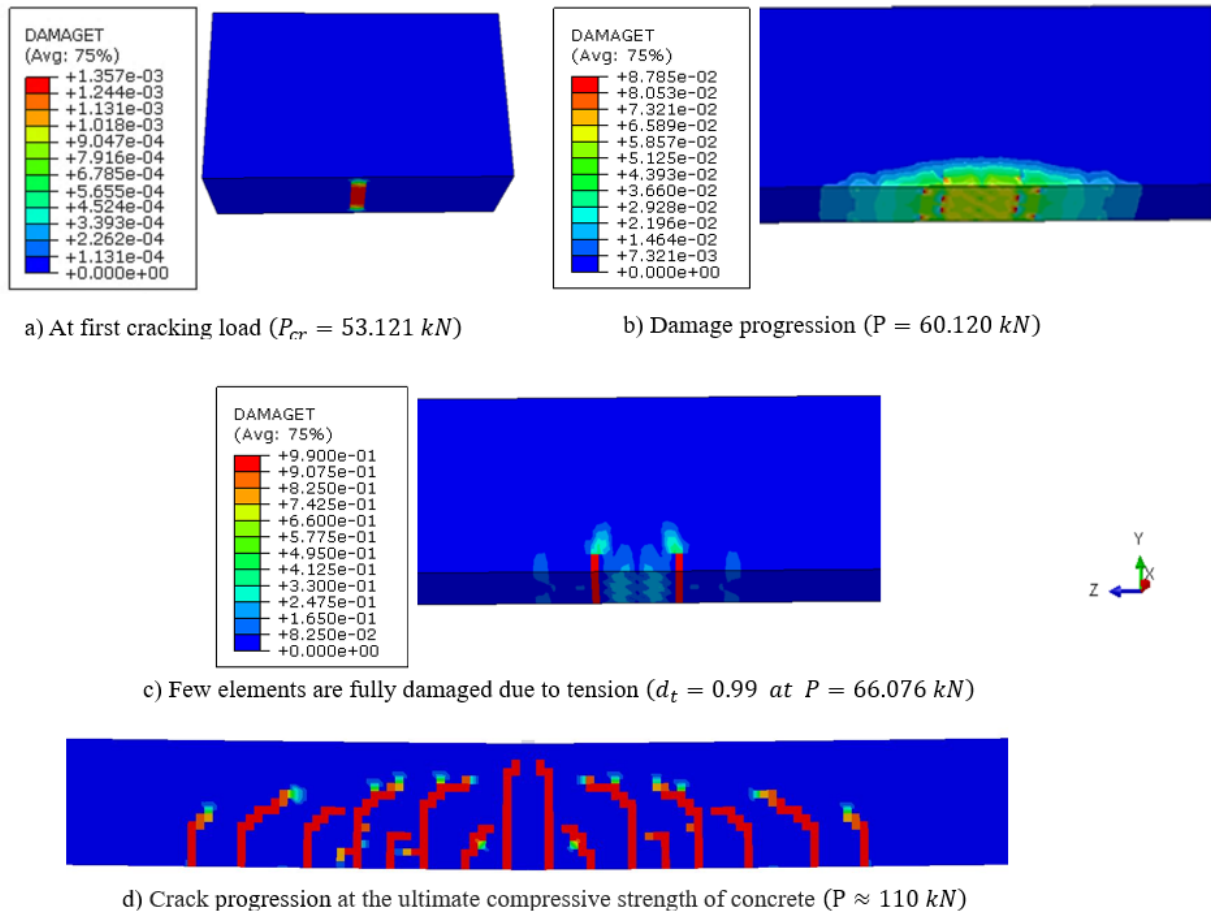
a) At first cracking load ($P_{cr} = 53.121 \ kN$)

b) Damage progression (P = 60.120 kN)

c) Few elements are fully damaged due to tension ($d_t = 0.99 \ at \ P = 66.076 \ kN$)

d) Crack progression at the ultimate compressive strength of concrete (P $\approx$ 110 kN)

Fig. 17. Development of beam cracks at mid-span at various loading stages – Model AP-M18-06

6. CONCLUSIONS

The study presents a comprehensive and rigorous framework for the analytical and numerical analysis of prestressed concrete beams, offering detailed guidance on their behaviour during various stages. The findings revealed that the studied parameters substantially influenced capturing the deflection and stresses at the mid-span of prestressed concrete beams, highlighting the challenges in capturing real-world phenomena accurately. The numerical model has been optimized step by step to match the analytical calculations. For this purpose, several parameters were investigated, including mesh sizes, meshing strategies, element type, and prestressing method. The findings showed a significant impact of these parameters on the numerical results.

- It is essential to compare numerical results with analytical solutions, if available, to ensure the model's accuracy. Additionally, analytical and numerical solutions together help us better understand structural behavior and the physics behind it. This approach provides a clear framework for predicting performance and enables a deeper understanding of how different factors influence the beam's response under various loading conditions.

- The results obtained were identical when applying prestressing force using either the initial stress or cooling methods.
- The outcomes revealed that the mesh size significantly impacts the accuracy of results; smaller mesh sizes yield greater accuracy in detecting deflection and stress.
- The meshing strategy used not only improved the accuracy of the numerical results but also strongly affected the convergence and computation time.
- The type of elements highly affected the numerical results. The C3D8I was more time-consuming but resulted in a noticeable improvement in the deflection and stresses in the elastic range. However, it's not recommended for use in the inelastic range with the CDP model due to producing unreasonable values. The C3D8R was more effective at detecting damages in accordance with CDP data in Tables 3 and 4.
- The study found that utilizing a finer mesh in models BT-M18-06 and AP-M18-06 proves beneficial for capturing behaviour from the elastic stage to the inelastic one, showcasing noteworthy deflection, stress, and cracking force results.
- The concrete damage plasticity model (CDP) is a powerful tool for simulating the structural responses of prestressed concrete beams at a nonlinear stage. The most common cause of non-convergence was the concrete material viscosity parameter, specifically at the hardening stage.
- Ideally, the viscosity parameter of the concrete material in the CDP model is set to zero. However, achieving convergence under these conditions is often unlikely for complex systems. Therefore, it is advisable to increase this value with caution, as increasing the viscosity parameter can significantly affect the results' accuracy, particularly at the beginning of the nonlinear region after the tensile damage reaches 0.99%.
- Future work will concentrate on enhancing the modeling of steel-concrete contact behavior to accurately represent bond-slip mechanisms and stress transfer at the interface. This will entail further refinement of the numerical model to incorporate advanced material properties and nonlinearities. Validation against experimental data will be crucial to ensure the model's accuracy and applicability, paving the way for more robust parametric analyses and practical applications.

ACKNOWLEDGMENTS

REFERENCES

1. Brandt, AM 2009. *Cement based composites: Materials, mechanical properties and performance*. 2nd ed. New York: Taylor & Francis.
2. Mehta, PK and Monteiro, PJM 2006. *Concrete, Microstructure, Properties, and Materials*. New York: McGraw-Hill.
3. Mosley, B, Bungey, J and Hulse, R 2009. *Reinforced Concrete Design to Eurocode* 2. London: Taylor & Francis.
4. Ulm F-J, Jennings, H M and Pellenq, R (Eds.), 2013. *Mechanics and Physics of Creep, Shrinkage, and Durability of Concrete – A Tribute to Zdeněk P. Bažant*. Cambridge, Mass.: ASCE.

5. Ajdukiewicz, A and Mames, J 2008. *Konstrukcje z betonu sprężonego* [*Structures from prestressed concrete*]. Kraków: Stowarzyszenie Producentów Cementu.
6. Knauff, M and Niedośpiał, M 2021. *Betonowe konstrukcje sprężone w budownictwie ogólnym* [*Prestressed concrete structures in building engineering*]. Warszawa: PWN.
7. Zienkiewicz, OC, Taylor, RL and Fox, DD 2014. *The Finite Element Method for Solid and Structural Mechanics* (Seventh Edition). Amsterdam: Butterworth-Heinemann.
8. Hillerborg, A, Modéer, M and Petersson, PE 1976. Analysis of crack formation and crack growth in concrete by means of fracture mechanics and finite elements. *Cement and Concrete Research* 6(6), 773-781.
9. Al-Hilali, AM and Izzet, AF 2023. 3D-Abaqus modelling of prestressed concrete hunched beams with multi-openings of different shapes. *Journal of Engineering* **29**(08), 149-170.
10. Yapar, O, Basu, P K and Nordendale, N 2015. Accurate finite element modeling of pretensioned prestressed concrete beams. Engineering Structures, 101, 163-178.
11. Lee, SH, Abolmaali, A, Shin, KJ and Lee, HD 2020. ABAQUS modeling for post-tensioned reinforced concrete beams. *Journal of Building Engineering* 30.
12. Wang, Z, Chen, M and Liao, Y 2023. Analysis of Fire Resistance of Prestressed Concrete T-Beam Based on ABAQUS Numerical Simulation. *Applied Sciences* 13(8).
13. EN 1992-1-1:2004, *Eurocode 2: Design of concrete structures Part 1-1: General rules and rules for buildings*.
14. *fib Model Code for Concrete Structures 2010*. Federation Internationale du Beton. Ernst & Sohn, 2013.
15. Derkowski, W and Dyba, M 2017. Behaviour of end zone of pre-tensioned concrete elements. *Procedia Engineering* **193**, 19-26.
16. Seruga, A and Jaromska, E 2012. Transmission length of tensioning force in prestressed panel elements. *Technical Transactions* **4-B**, 75-102.
17. Lubliner, J, Oliver, J, Oller, S and Onate, E 1989. A plastic-damage model for concrete. *International Journal of Solids and Structures* **25**(3), 299-326.
18. Lee, J and Fenves, GK 1998. Plastic-damage model for cyclic loading of concrete structures. *Journal of Engineering Mechanics* **124**(8), 892-900.
19. Hafezolghorani, M, Hejazi, F, bin Jaafar, MS and Adeli, H 2022. Plasticity model for partially prestressed concrete. *Structures* **38**, 630-651.
20. Jankowiak, T and Lodygowski, T 2005. Identification of parameters of concrete damage plasticity constitutive model. *Foundations of civil and environmental engineering* **6**(1), 53-69.
21. Grassl, P, Xenos D, Nyström, U, Rempling, R and Gylltoft, K 2013. CDPM2: A damage-plasticity approach to modelling the failure of concrete. *International Journal of Solids and Structures* **50**(24), 3805–3816.
22. Elharouney, O, Elkateb, M and Khalil, A 2021. Behavior of prestressed hollow core slabs strengthened with NSM CFRP strips around openings: A finite element investigation. *Engineering Structures* **238**.
23. Mercan, B, Schultz, AE and Stolarski, HK 2010. Finite element modeling of prestressed concrete spandrel beams. *Engineering Structure* **32**(9), 2804-2813.
24. Ren, W, Sneed, LH, Yang, Y and He, R 2015. Numerical simulation of prestressed precast concrete bridge deck panels using damage plasticity model. *International Journal of Concrete Structures and Materials*, **9**(1), 45-54.
25. Tuo, L, Jiang, Q and Chengqing, L 2008. Application of damaged plasticity model for concrete. *Structural Engineers* **24**(2), 22-27.

26. Garg, AK and Abolmaali, A 2009. Finite-element modeling and analysis of reinforced concrete box culverts. *Journal of Transportation Engineering* **135**(3), 121-128.
27. Abaqus/CEA User's Manual 6.12 (http://orpheus.nchc.org.tw:2080/v6.12/index.html).
28. Drucker, DC and Prager, W 1952. Soil mechanics and plastic analysis or limit design. *Quarterly of Applied Mathematics* **10**(2), 157-165.
29. Szczecina, M and Winnicki, A 2015. Calibration of the CDP model parameters in Abaqus. World Congress on Advances in Structural Engineering and Mechanics (*ASEM15*), August 25-29, 2015, Incheon, Korea.
30. Hafezolghorani, M, Hejazi, F, Vaghei, R, bin Jaafar, MS and Karimzade, K 2017. Simplified damage plasticity model for concrete. *Structural Engineering International* **1**, 68-78.
31. Hasan, Al-R and Darbaz, M 2022. Comparative assessment of commonly used concrete damage plasticity material parameters. *Engineering Transactions* **70**(2), 157-181.
32. Kuczma, M and Whiteman JR 1995. Variational inequality formulation for flow theory plasticity. *International Journal of Engineering Science* 33(8), 1153-1169.
33. Tabrizikahou, A, Białasik, J, Borysiak, S, Fabisiak, M, Łasecka-Plura, M, Jesionowski, T and Kuczma, M 2024. Shear strengthening of damaged reinforced concrete beams with iron-based shape memory alloy (Fe-SMA) strips: numerical and parametric analysis. *Archives of Civil and Mechanical Engineering* **24:**189.
34. Bílý, P and Kohoutková, A 2015. Sensitivity analysis of numerical model of prestressed concrete containment. *Nuclear Engineering and Design* **295**, 204-214.
35. Deng, L, Ghosn, M, Znidaric, A and Casas, JR 2001. Nonlinear flexural behavior of prestressed concrete girder bridges. *Journal of Bridge Engineering* **6**(4), 276-284.
36. Mezher, A, Jason, L, Folzan, G and Davenne, L 2022. Simulation of large dimensional reinforced and prestressed concrete structures using a new adaptive static condensation method including automatic mesh partitioning. *Finite Elements in Analysis & Design* 202, 103718.